SUPPLEMENTAL MATERIAL

The role of the westerlies and orography in Asian hydroclimate since the late Oligocene

Xin Wang*, Barbara Carrapa, Yuchen Sun, David L. Dettman, James B. Chapman, Jeremy K. Caves Rugenstein, Mark T. Clementz, Peter G. DeCelles, Mi Wang, Jie Chen, Jay Quade, Fei Wang, Zaijun Li, Ilhomjon Oimuhammadzoda, Mustafo Gadoev, Gerrit Lohmann, Xu Zhang, and Fahu Chen*

ADDITIONAL DETAILS ON METHODS AND RESULTS

1. Stable Isotope Geochemistry Method.

In the Tajik Basin, bulk mudstone and fine sandstone samples were collected from the continental redbed in the CD (n=10) and PE (n=62) sections for stable oxygen and carbon isotope analyses. One oyster fossil, namely Ostrea *Kalizky Vialov* (Popov personal communication), was collected from the Bukhara Fm. in the base of the CD section in order to evaluate potential diagenetic processes and primary seasonal $\delta^{18}O$ variability. Soil carbonate nodules were not found in the studied sections, but were collected from the upper Eocene Shurysay member in the ZD section (n=8) and the Miocene Chingou Fm. in the DS (n=3) section for comparison (See Fig. 1 for location). In the western Tarim Basin, 25 samples at an average spacing of 3 m were collected from Paleogene sequences in the UL section.

Thin sections of sandstone samples were examined microscopically to identify regions with fewer than normal authigenic carbonate lithics that can be preferentially drilled for stable isotope analysis. Point counting analysis was performed on each thin section in order to calculate the intergranular volumes (IGV) and the relative proportion of carbonate cements and extrabasinal carbonate lithic (detrital carbonates) within the samples. All calculations are based on ~500 total points counted for each sample. These

points were classified as framework grains and interstitial material. The latter was further subdivided into cement, pore space, and matrix. The IGV of a sandstone sample is defined as the volume of interstitial material divided by the total rock volume (Paxton et al., 2002). The extrabasinal carbonate lithics content of a sample is expressed as the ratio of extrabasinal carbonate lithic grains to the carbonate cement count, and the ratio of extrabasinal carbonate grains to total framework grains. Two pilot samples, with relatively high extrabasinal carbonate lithic proportions, were selected from the lower and upper part of the PE section. The hand-block samples were firstly polished and scanned under a Hitachi 3400N Scanning Electron Microscope (SEM) equipped with an Oxford Energy-dispersive X-ray spectroscopy (EDS) system to identify regions of pure carbonate cement, which was then drilled using a dental drill under a binocular microscope.

Stable isotope analyses were performed at both the Key Laboratory of Western China's Environmental Systems, Lanzhou University and the Environmental Isotope Laboratory at the University of Arizona. In the Lanzhou University system, a few milligrams of powdered sample were placed in a sealed reaction vessel, which was then flushed with helium and then reacted with 100% phosphoric acid at 72 °C. Carbon dioxide was then sampled from the vessels using a Finnigan Gas-Bench, and stable oxygen and carbon isotope ratios were measured using a Finnigan MAT Delta plus XL mass spectrometer. Repeated analysis of NBS-19 and Merck standards indicates that the laboratory precision of both oxygen and carbon isotope ratios is better than 0.2‰. At the University of Arizona, the $\delta^{18}O$ and $\delta^{13}C$ values of carbonates were measured using an automated carbonate preparation device (KIEL-III) coupled to a gas-ratio mass spectrometer (Finnigan MAT 252). Powdered samples were reacted with dehydrated phosphoric acid under vacuum at 70°C. The isotope ratio measurement is calibrated

based on repeated measurements of NBS-19 and NBS-18 and precision is ± 0.1 ‰ for $\delta^{18}O$ and ±0.08‰ for $\delta^{13}C$ (1sigma). $\delta^{13}C$ values of organic matter were measured on a continuous-flow gas-ratio mass spectrometer (Finnigan Delta PlusXL) coupled to an elemental analyzer (Costech) at the Environmental Isotope Laboratory at the University of Arizona. Standardization is based on acetanilide for elemental concentration, NBS-22 and USGS-24 for $\delta^{13}C$, and precision is better than ± 0.10 ‰.

2. Measurement of geochemical elements and calculation of Chemical proxy of alteration (CPA).

We focus our effort on fine-grained samples (particle size < 55 μm), because size sorting during transportation and deposition led to some degree of mineralogical differences, which may modify the CPA values. For geochemical analysis, the concentrations of 32 major, trace and rare earth elements/oxides (Cl, S, P, As, Ba, Ce, Co, Cr, Cu, Ga, Hf, La, Mn, Nb, Nd, Ni, Pb, Rb, Sr, Th, Ti, Tl, V, Y, Zn, Zr, Fe_2O_3, SiO_2, Al_2O_3, CaO, Na_2O, K_2O) were determined using a PANalytical PW2403/00 X-ray fluorescence spectrometer. CIA values were calculated using the formula: $CPA=Al_2O_3/(Al_2O_3+ Na_2O)\times100$ (in molar proportions) (Buggle et al., 2011).

3. Clay mineral analysis.

We apply X-ray diffraction (XRD) analysis to identify clay minerals in the sedimentary rocks and scanning electron microscopy (SEM) observations to determine their origin. For XRD analysis, we isolated clay fractions by sedimentation method as described by ref Jackson (2005). Each sample was subdivided into four slides with different treatments, namely Mg-saturation, Mg-saturation in combination with saturation of glycerol, K-saturation, K-saturation combined with heating to 550 °C for 1h. Clay slides were scanned on an X-ray diffractometer from 3 to 30° with a step size

of 0.02° 2θ/step and speed of 2 s/step, under 45 kV and 30 mA working conditions. The clay minerals were determined by characteristic reflections in XRD patterns (Moore and Reynolds, 1989). For SEM observations, blocks of the selected samples were platinum-coated, and then, were observed on a Hitachi 3400N scanning electron microscope at an accelerating voltage of 13-15 kV. XRD analysis was performed at Lanzhou University and SEM observations were performed both at the university of Arizona and Lanzhou University.

4. Climate model simulation method.

We use an Atmosphere General Circulation Model (AGCM), ECHAM5 (Stepanek and Lohmann, 2012), to evaluate the role of topographic changes in Pamir and Tian Shan in climate during the Late Oligocene. ECHAM5 was adapted for climate research from the weather forecasting model of the European Centre for Medium-Range Weather Forecasts (ECMWF) and developed at the Max Planck Institute in Hamburg (Germany). The model is based on a spectral dynamical core and simulates the troposphere and the lower stratosphere up to a pressure level of 10 hPa. The vertical dimension is organized on a hybrid sigma-/pressure-level system. In our model setup, we use ECHAM5 in T106/L31 resolution (i.e. there are 31 levels present and triangular truncation of the series of spherical harmonics is performed at wave number 106).

We design the Pre-industrial (EXP.PI) and the Late Oligocene (EXP.LO) experimental groups to portray the annual precipitation and its $\delta^{18}O$ over Central Asia. The PI experimental group using boundary conditions of pre-industrial period (Stepanek and Lohmann, 2012), whereas the EXP.LO experimental group with additional change in the land-sea distribution in Euroasia (i.e. large area extent of the Paratethys during Late Oligocene) (Fig. S6, Table S3), following the dataset from

Markwick (2007), which is overall agreement but slightly larger than paleogeographic reconstructions (Popov et al., 2004; Bosboom et al., 2017).

To better understand the impact of tectonic uplift on climate changes over central Asia and constraining the threshold altitude of the mountains that could block westerlies moisture, we conducted sensitivity simulations with progressive height reductions in the Pamir-Tian Shan convergence zone (64ºE-78 ºE, 34.5 ºN-43.5 ºN) for the EXP.PI and EXP.LO experimental group, respectively (Fig. S6, Table S3).

5. Stable Carbon isotope records and its interpretations

5.1 Results

Carbon isotope compositions of nonmarine strata ($\delta^{13}C_{cc}$) in the Tajik Basin range from -4.59 to 0.22‰, whereas, the coexisting organic matter has $\delta^{13}C$ values ($\delta^{13}C_{org}$) that fall between -27.05 and -24.19‰ (Fig. S7). Both records yield a slightly stepwise increasing trend up-section. $\delta^{13}C_{cc}$ values of carbonate nodule samples from the upper Eocene strata in the adjacent Zadi (ZD) section and the upper Oligocene to lower Miocene strata in the Dashtijum section (DS) averaged at -6.18 and -4.33‰ and are systematically lower than those of the cements samples (Fig. S7).

5.2 Evaluating the $\delta^{13}C_{cc}$ records and its paleoclimate implication

Shallow surface water or groundwater bicarbonate will control the $\delta^{13}C_{cc}$ values of fluvial cements; and it may be derived from the dissolution of limestone or a mixture of other sources. In contrast, the carbon isotope ratios of paleosol carbonate and organic matter are widely used as proxy indicator for paleoecology and paleoclimate changes in terrestrial depositional systems (Cerling et al., 1989). Paleosol $\delta^{13}C_{cc}$ values are controlled by the isotopic composition of soil-respired CO_2, which depends mainly on the photosynthetic pathway of the overlying plants, and on climatic changes where the soil respiration rates are high (Cerling, 1984). Organic matter in soils and sediments

has a carbon isotopic composition derived from local plant matter, which also depends on photosynthetic pathway. C3, C4, and crassulacean acid metabolism (CAM) plants exhibit different carbon isotopic compositions, ranging from -22‰～-30‰, -9‰～-19‰, and -14~-34‰ (O'Leary, 1988), respectively. For example, paleosol carbonates precipitated in equilibrium with CO_2 derived solely from C3 plants have $\delta^{13}C_c$ values ranging from -9 to -13‰, and are associated with organic matter that have $\delta^{13}C_{org}$ values typically ≤ −24‰ (Cerling, 1984).

$\delta^{13}C_{org}$ values in the Tajik Basin fall between -27.05 and -24.19‰ (Fig. S7), indicating that the overlying vegetation type was made entirely by C3 plants. It is important to note, however, that the carbon isotope ratio difference between cements and associated organic matter is much larger than the expected difference for soil carbon isotope ratios. Instead of the typical 14‰ to 16‰ difference, cements and coexisting organic matter have $\delta^{13}C$ values that differ by 22.5 to 25.6 ‰. This suggests that the $\delta^{13}C_{cc}$ values obtained from cements in this study are strongly affected by groundwater DIC rather than CO_2 derived from the soil. The $\delta^{13}C_{cc}$ values of cements in this study, therefore, have little to do with the regional climate.

The $\delta^{13}C$ values of soil carbonate nodule samples from upper Eocene strata in the ZD section and the upper Oligocene to lower Miocene strata in the DS section have average values between -6.18 and -4.33‰, which are systematically higher than the typical $\delta^{13}C$ values from a pure C3 source (c.a. -11‰). These surprisingly high carbon isotope ratios, commonly observed in arid central Asia, may have arisen from very low soil-respiration-rates due to limited primary productivity (Caves et al., 2016). This leads to elevated $\delta^{13}C_{cc}$ values because of mixing with the atmospheric CO_2 and perhaps the water-stress effect on plant with effects on $\delta^{13}C$ values (Caves et al., 2016). Because both of these factors are caused by arid climate conditions, we infer that an arid climate

had been established in the Tajik Basin since at least the late Eocene.

ADDITIONAL REFERENCES CITED

Cerling, T., Quade, J., Wang, Y., and Bowman, J., 1989, Carbon isotopes in soils and palaeosols as ecology and palaeoecology indicators: Nature, v. 341, no. 6238, p. 138-139.

Cerling, T. E., 1984, The stable isotopic composition of modern soil carbonate and its relationship to climate: Earth and Planetary Science Letters, v. 71, no. 2, p. 229-240.

Jackson, M. L., 2005, Soil chemical analysis: advanced course, UW-Madison Libraries Parallel Press.

Moore, D. M., and Reynolds, R. C., 1989, X-ray Diffraction and the Identification and Analysis of Clay Minerals, Oxford university press Oxford.

O'Leary, M. H., 1988, Carbon isotopes in photosynthesis: Bioscience, v. 38, no. 5, p. 328-336.

Berger, A., 1978, Long-Term Variations of Daily Insolation and Quaternary Climatic Changes: Journal of the Atmospheric Sciences, v. 35, no. 12, p. 2362-2367.

Wei, W., and Lohmann, G., 2012, Simulated Atlantic Multidecadal Oscillation during the Holocene: Journal of Climate, v. 25, no. 20, p. 6989-7002.

Zhang, X., Lohmann, G., Knorr, G., and Xu, X., 2013, Different ocean states and transient characteristics in Last Glacial Maximum simulations and implications for deglaciation: Clim. Past, v. 9, no. 5, p. 2319-2333.

SUPPLEMENTAL FIGURES

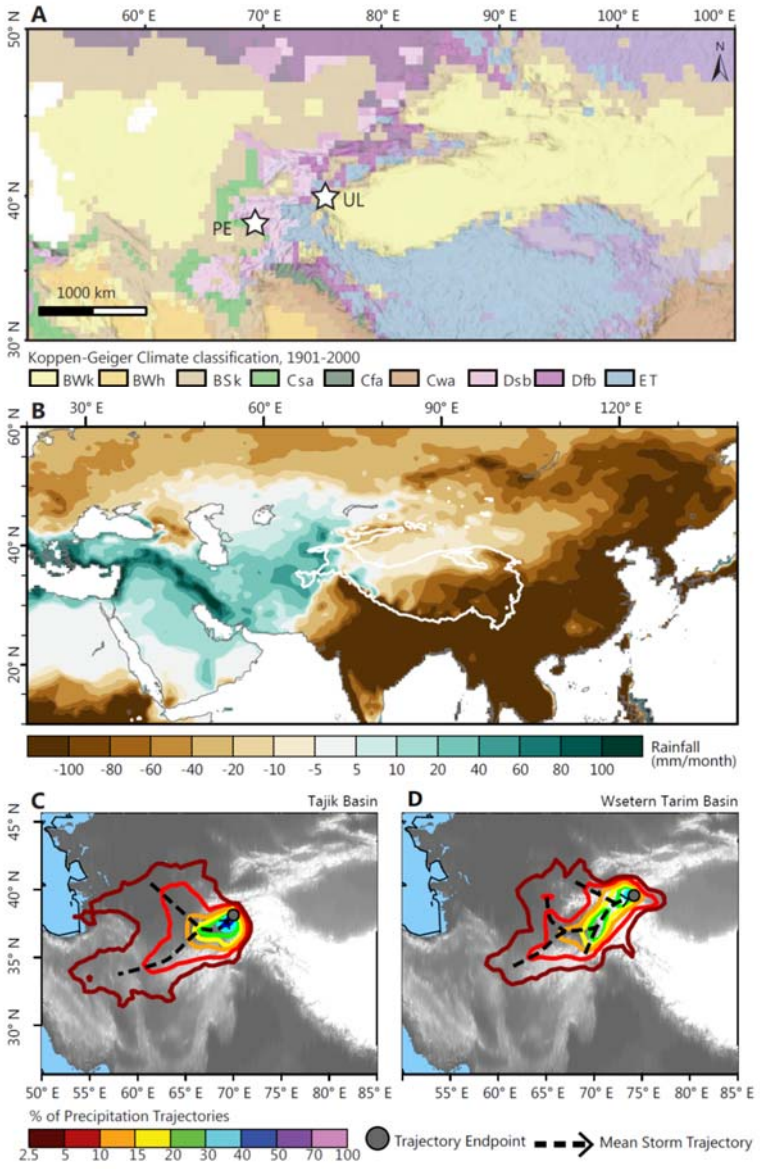

Fig. S1. Climatic setting over central Asia. (**A**) Koppen-Geiger climate classification of the mid-latitude Euro-Asia (https://www.arcgis.com), showing the west-east environment differences over central Asia. (**b**) Seasonal precipitation differences between boreal winter (DJF) and summer seasons (JJA) based on the NCEP/NCAR atmospheric reanalysis data (Kalnay et al., 1996) during 1971-2000. (**C-D**) Contours of precipitation-producing storms over the Tajik and the western Tarim basins. Mapped using the Hybrid Single-Particle Lagrangian Integrated Trajectory Model (HYSPLIT) (Caves et al., 2015). Note that nearly all precipitation-producing storms originate to the west, indicating the westerlies moisture plays a leading role in controlling hydroclimate changes in the working sections.

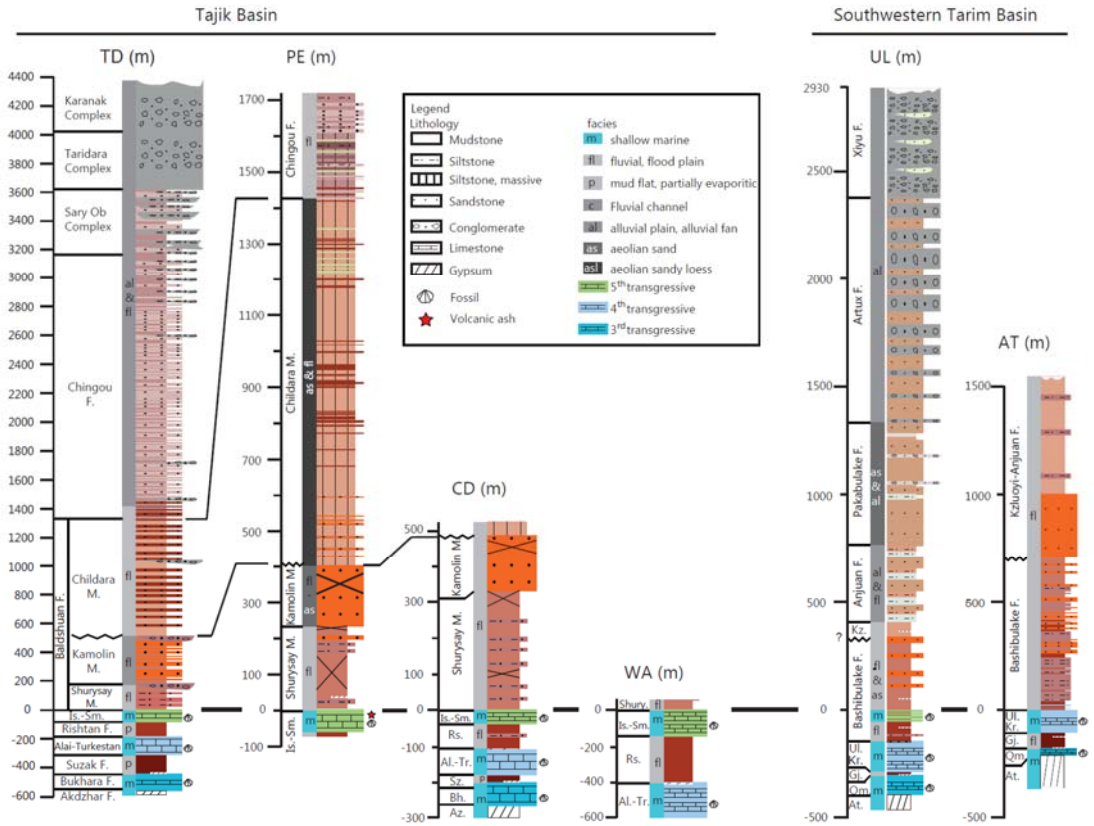

184

185 **Fig. S2. Stratigraphy of the Cenozoic sequences in the Tajik and the western**
186 **Tarim basins** (after Wang et al., 2019 and references there in). The correlation is based
187 on lithology, paleontology, and regional stratigraphic subdivisions. Zero level is
188 defined by the top of the stratigraphically highest shallow marine strata for comparing
189 purpose. Abbreviations for formation/member name: Az.-Akdzha; Bh.-Bukhara; Sz.-
190 Suzak; Al.-Alai; Tr.-Turkestan; Rs.-Rishtan; Is.-Isfara; Sm.-Sumsar; Shury.-Shurysay;
191 At.-Aertashi; Qm.-Qimugen; Gj.-Gaijitage; Kr.-Karatar; Ul.-Ulagen; Kz.-Keziluoyi.

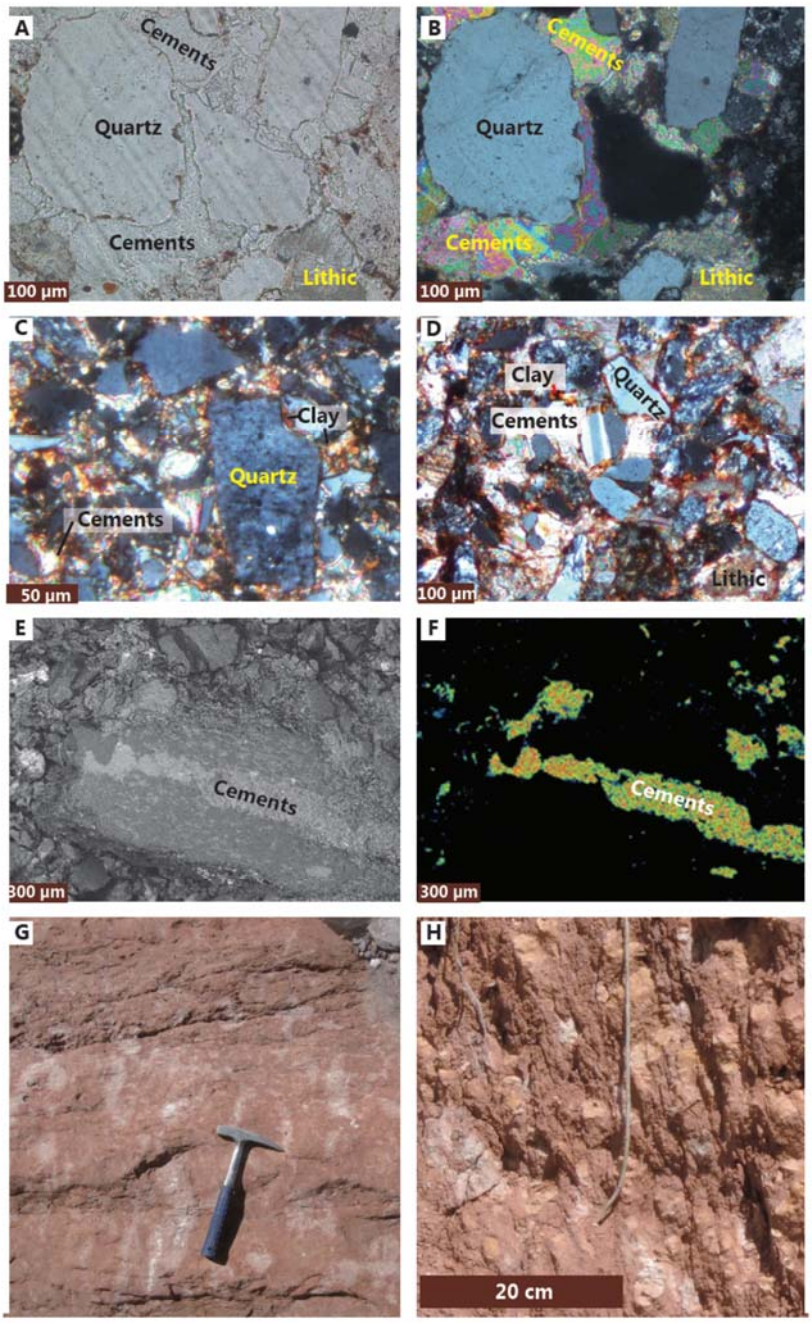

Fig. S3. Petrographic images showing the compositions of carbonate materials. Thin section photography of a sandstone samples under PPL (**A**) and XPL (**B**), showing both carbonate cements and lithics preserved in the samples. (**C-D)** Micromorphology of silt stone samples from the PE section, showing weakly-developed pedogenic features such as illuvial clay (**C**) and calcite crystallite b-fabric (**D**) within the samples. (**E-F**) Scanning Electron Microscope (SEM) image (**E**) and Energy-dispersive X-ray spectroscopy (EDS) showing distribution of element Ca surrounding a quartz, indicating pure carbonate cements which were drilled for stable isotope analysis. (**G-H**), photography of shows paleosol carbonate nodule in the Miocene Chingou Fm. from the DS section (**G**) and the Upper Eocene Shurysay Member in the CD section (**H**).

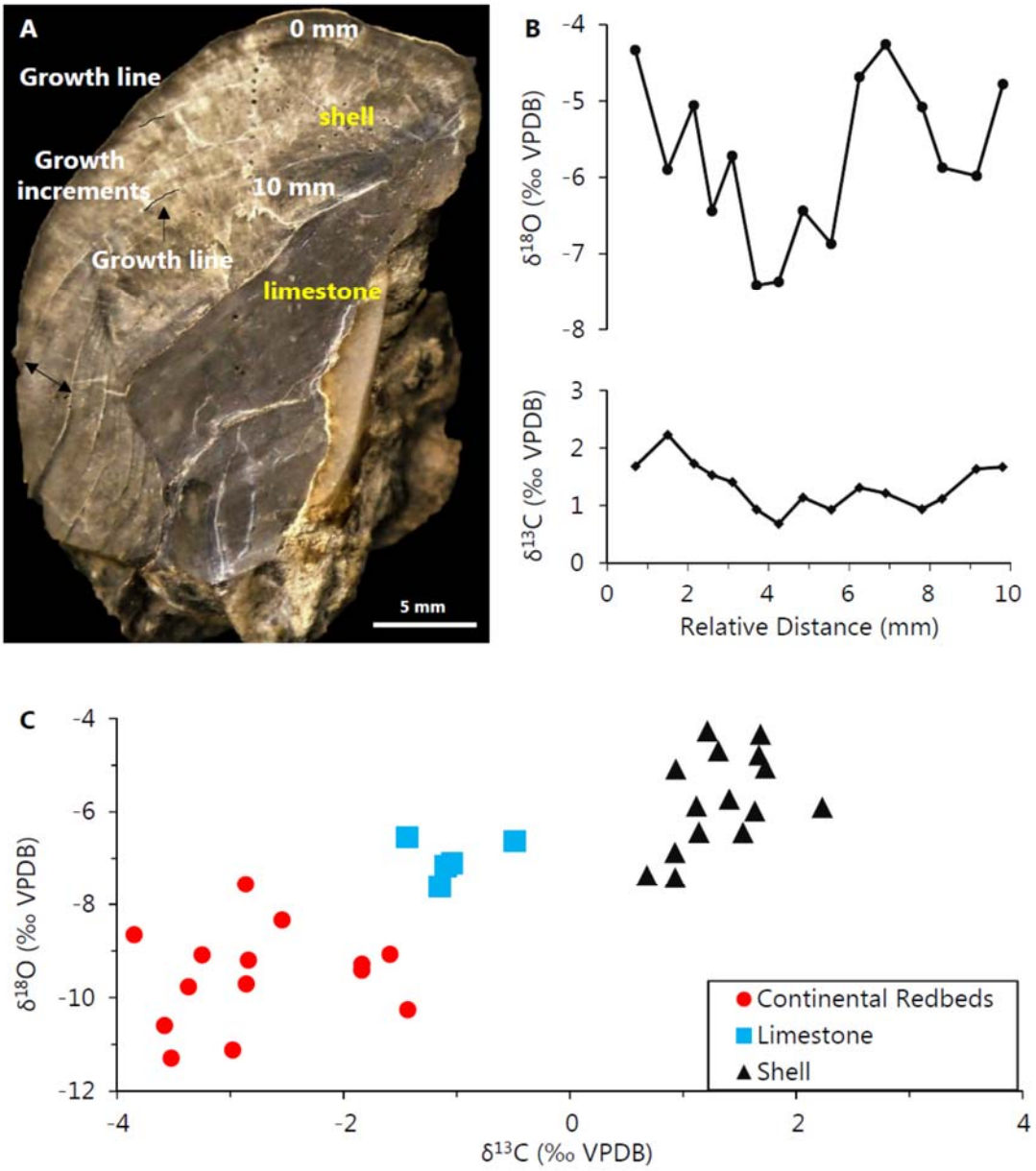

203

204 **Fig. S4. High-resolution $\delta^{18}O$ and $\delta^{13}C$ of an Oyster fossil.** (**A**) Polished cross
205 sections of Ostrea *kalizky Vialov* revealing annual growth bands. (**B**) high-resolution
206 $\delta^{18}O$ and $\delta^{13}C$ values along a growth line of the shell. Distance is measured from the
207 first drilled micro-sample at the edge of the shell. (**C**) Cross plot of $\delta^{18}O$ versus $\delta^{13}C$
208 for the Oyster fossils, limestone, and adjacent continental red beds in the lower part of
209 the studied sections. The differences between different type of sediments indicate
210 limited diagenetic alteration.

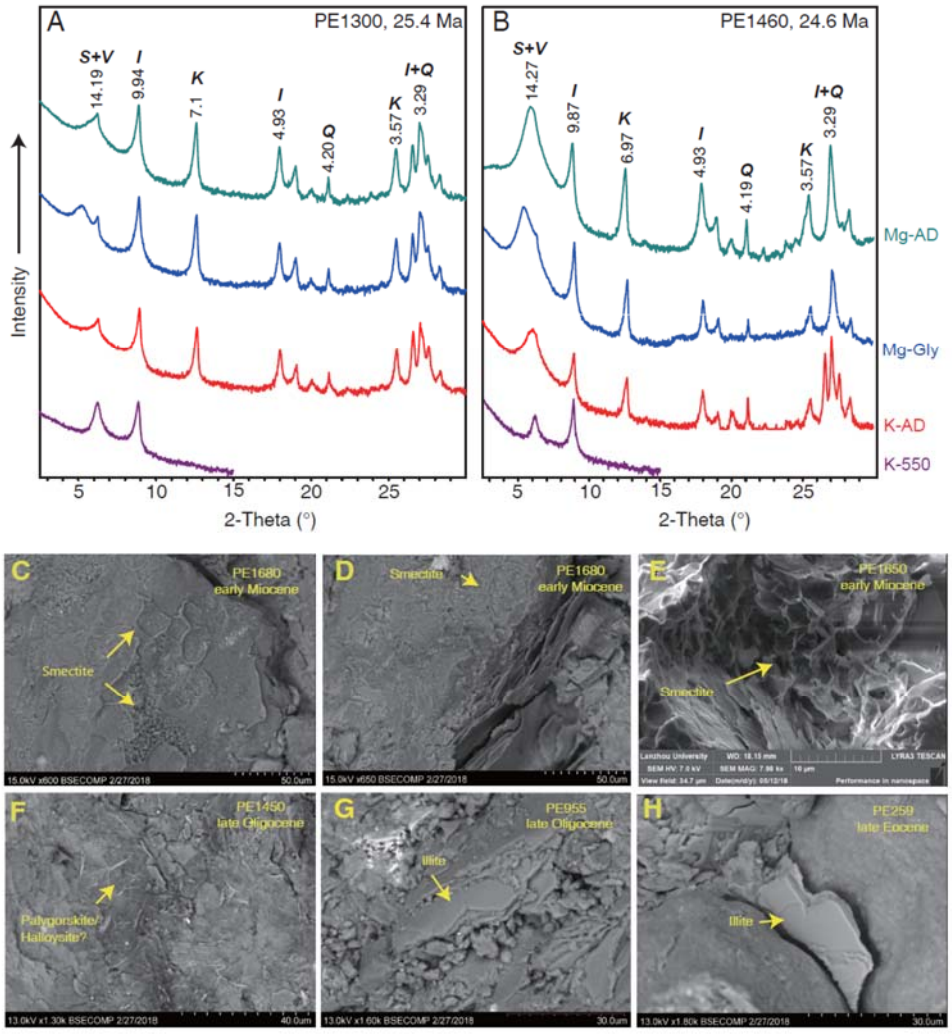

211

212 **Fig. S5. Clay mineral records.** (**A-B**) Example of multi-treatment X-ray diffraction
213 (XRD) patterns of representative sample from the PE section. S: smectite, I: illite, K:
214 kaolinite, V: vermiculite; Ch: chlorite, Q: quartz, Mg-AD: magnesium saturated and
215 air-dried; Mg-Gly: magnesium and glycerol saturated; K-AD: potassium saturated and
216 air-dried; K-550: potassium saturated and 550 °C heating. (**C-H**) SEM image of clay
217 minerals.

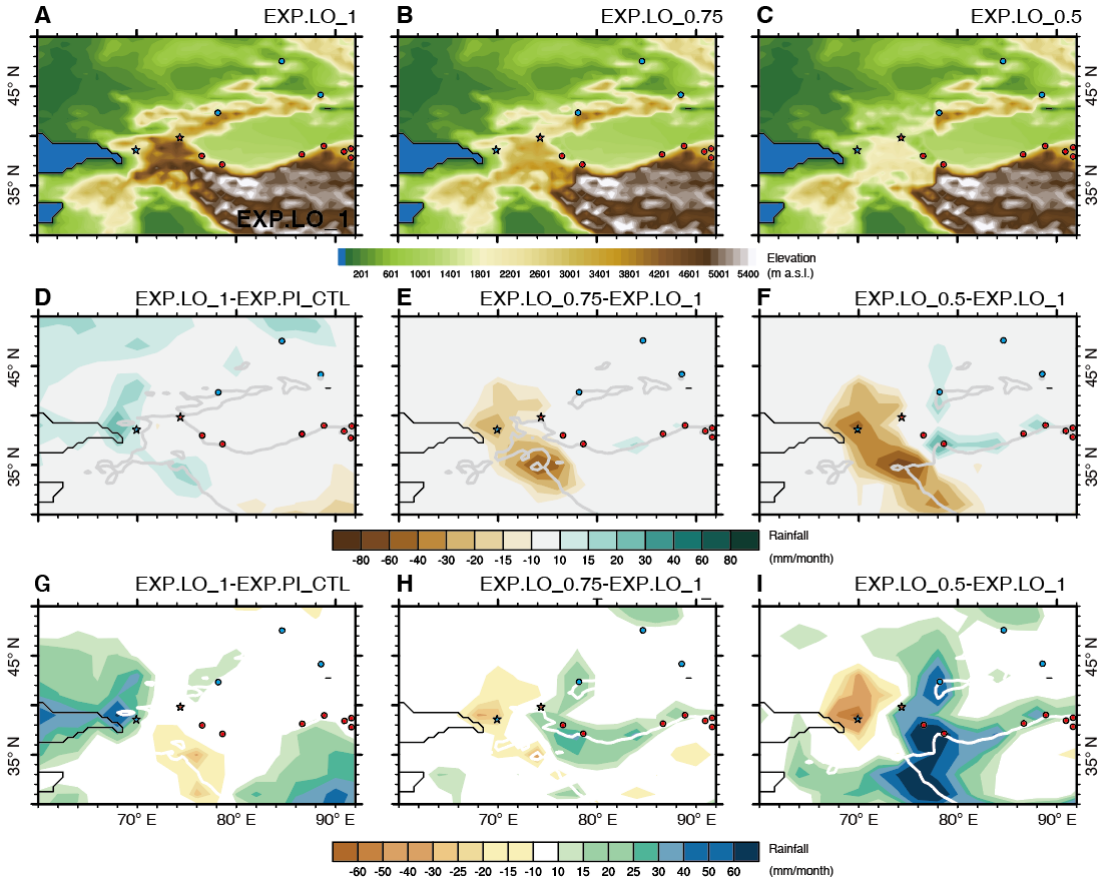

Fig. S6. Climatic simulations. (**A-C**) Topographies and ocean bathymetries designed for high mountains (100% relief, ~4000 m), medium mountain (75% relief, ~3000 m), and low mountain (50% relief, ~2000 m) scenarios. (**D**) Annual precipitation differences between Late Oligocene high mountains experiment and pre-industrial control experiment, showing the Late Eocene climate in central Asia is wetter than the pre-industrial period due to the presence of the Paratethys. (**E-F**) Annual precipitation differences between Late Oligocene medium (low) mountain and high mountains experiment, revealing decreases precipitation in the mountain regions and its western front, and increases precipitation in the eastern side associated with reducing topography in the Pamir-Tian Shan convergence zone. (**G**) Seasonal precipitation differences between Late Oligocene high mountains experiment and pre-industrial control experiment. (**H-I**) Seasonal precipitation differenced between Late Oligocene medium (low) mountain and high mountains experiment, suggesting that the east-west seasonal precipitation differences become much weaker associate reduction of elevations in the Pamir-Tian Shan convergence zone.

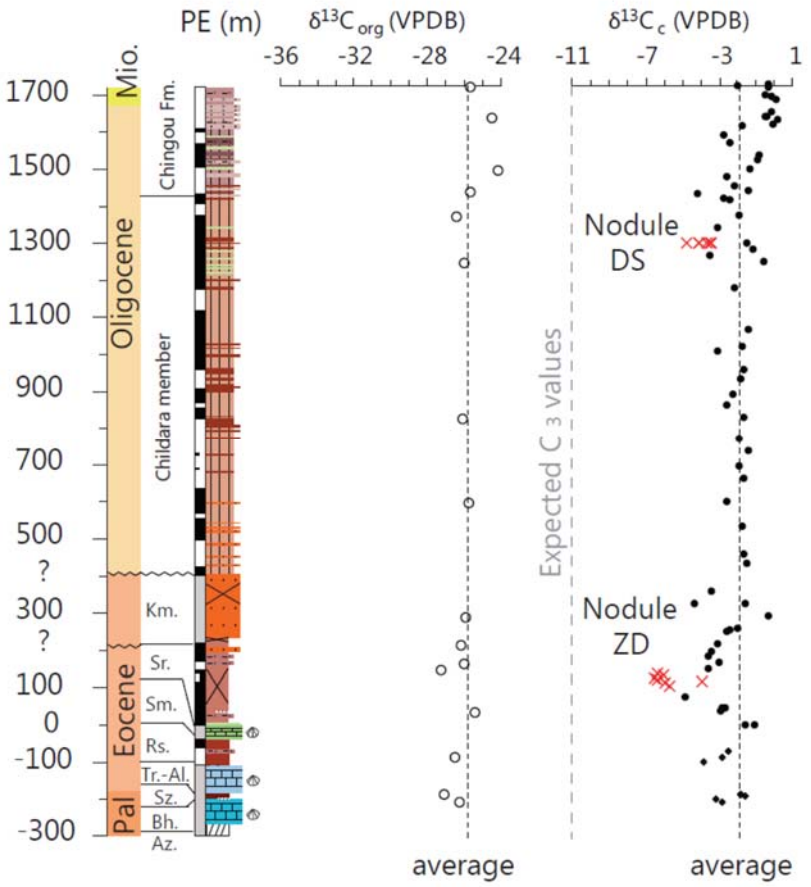

234

235 **Fig. S7. Stable carbonate isotope of the early Cenozoic sequences in the Tajik**
236 **Basin.** The $\delta^{13}C$ values of paleosol carbonate from the DS and ZD sections are indicated
237 by red cross for comparison. $\delta^{13}C$ values of soil carbonate nodule samples have average
238 values between -6.18 and -4.33‰, which are systematically higher than the typical δ
239 ^{13}C values from a pure C3 source (c.a. -11‰), which may have arisen from very low
240 soil-respiration-rates due to limited primary productivity, which are caused by arid
241 climate conditions. Note that the carbon isotope ratio difference between cements and
242 associated organic matter is much larger than the expected difference (~14‰ to 16‰)
243 for soil carbon isotope ratios. This suggests that the $\delta^{13}C_{cc}$ values obtained from
244 cements in this study are strongly affected by groundwater dissolved inorganic carbon
245 (DIC) rather than CO_2 derived from the soil. The $\delta^{13}C_{cc}$ values of cements in this study
246 thus have little to do with the regional climate.
247

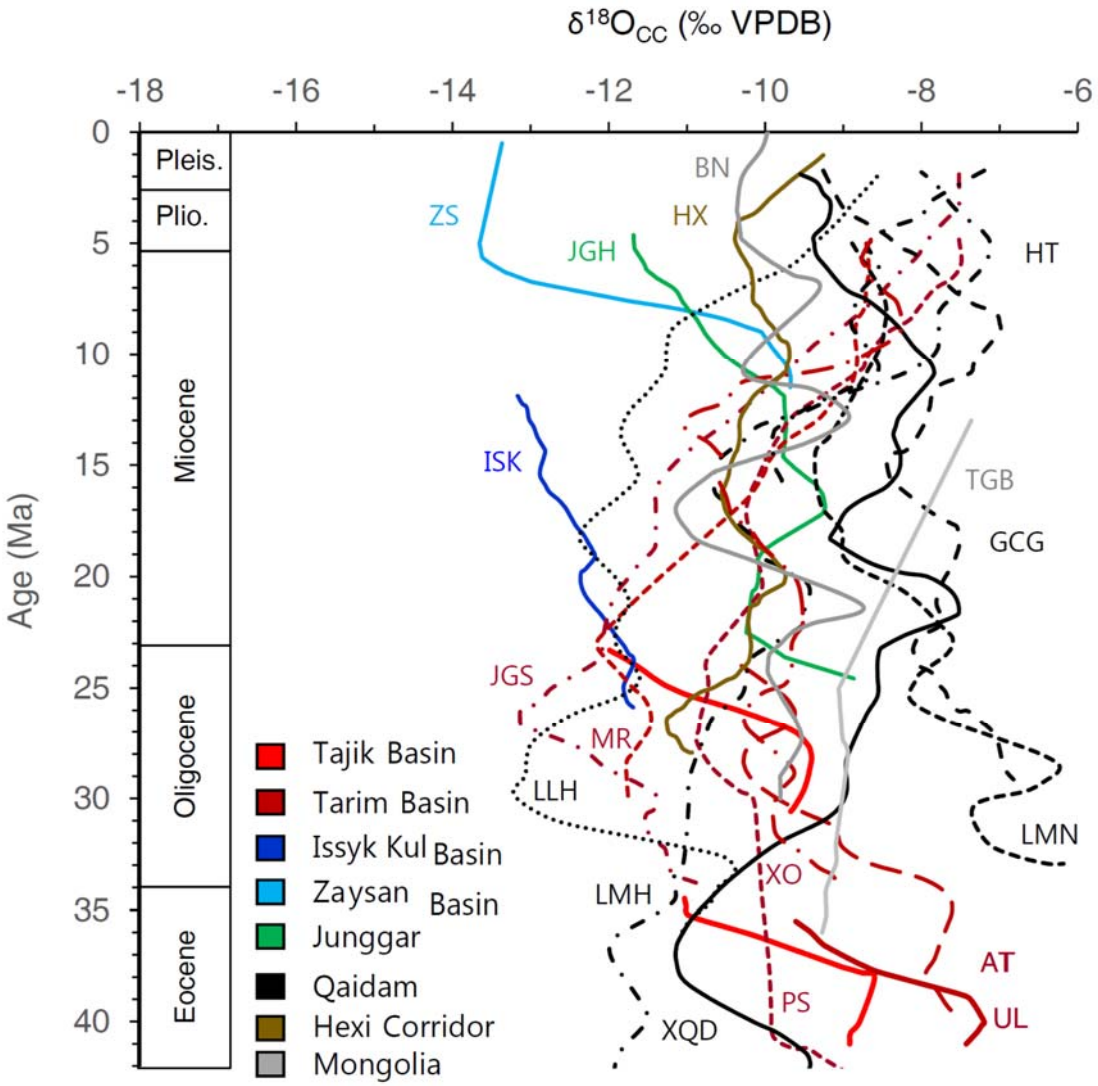

248

249 **Fig. S8. Citations of $\delta^{18}O_{cc}$ records.** Data from each section were smoothed using
250 an Epanechnikov kernel with a 1 Ma bandwidth. Colored lines correspond to different
251 basins. ISK-Issyk Kul (Macaulay et al., 2016), ZS-Zaysan (Caves et al., 2017), JGH-
252 Jingouhe (Charreau et al., 2012); HT-Huaitoutala (Zhuang et al., 2011); BN= Biger
253 Noor, TGB-Taatsin Gol (Caves et al., 2014); AT-Aertashi, PS-Puska, MR-Miran River,
254 JGS-Janggalsay, XO-Xorkol, HX- Hexi Corridor, GCG-Ganchaigou, LLH-Lulehe,
255 LMH-Lake Mahai, LMN-Laomangnai, XQD- Xiao Qaidam (Kent-Corson et al., 2009).

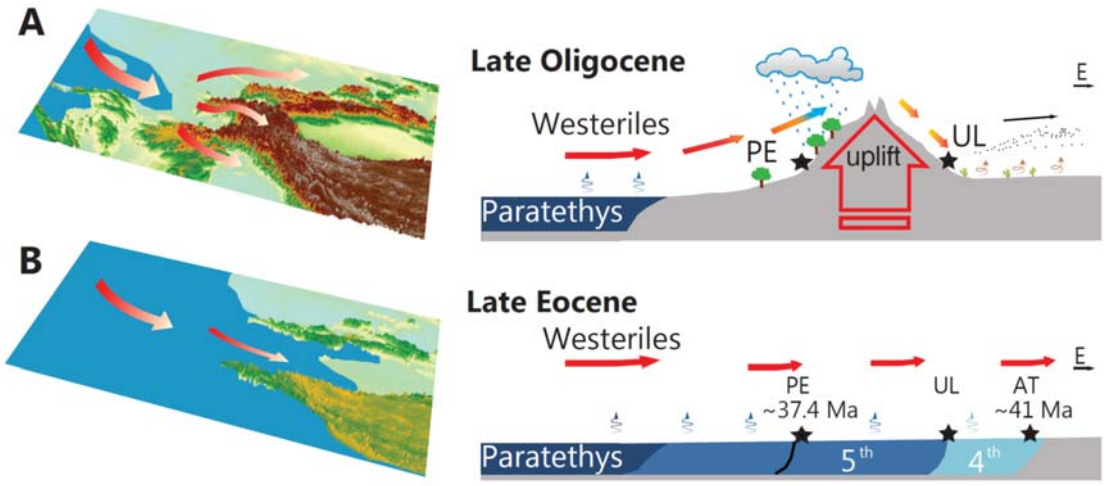

256

257 **Fig. S9. Schematic models showing topographic-atmospheric configuration**
258 **changes over central Asia during the Cenozoic.**

259

SUPPLEMENTAL TABLE CAPTIONS

Table S1. **Stable isotope data** (provided as excel format).

Table S2. CPA data, calculated from fine-grained samples, in the Tajik Basin (provided as excel format).

Table S3. Boundary conditions in climate simulations. The topography of the Pamir-Tian Shan convergence zone (64ºE-78 ºE, 34.5 ºN-43.5 ºN) was expressed as a percentage to modern elevation and approximate height. Land-sea distribution during the late Oligocene was cited from Markwick (2007). Orbital parameters are calculated according to Berger (1978). The pre-industrial (PI) climate boundary conditions are set from a PI simulation, which has been run into equilibrium over several thousand years (Wei et al., 2012; Zhang et al., 2013).

Experiment ID	Topography	Land-sea	Orbital	CO_2 (ppm)	CH_4 (ppb)	N_2O (ppb)	SST Ice volume Sea level
EXP.LO_1	100% / 4000m	Late Oligocene	PI	280	760	270	PI
EXP.LO_2	75% / 3000m	Late Oligocene	PI	280	760	270	PI
EXP.LO_3	50% / 2000m	Late Oligocene	PI	280	760	270	PI

280 **Table S4. Sandstone point counting results.**

281

Stratigraphic Position (m)	Total Counts	Extra-basinal	Cement	Matrix	Pore	IGV (%)	Extralbasinal/ Cement (%)	Extralbasinal /Total (%)
PE250	500	15	96	33	4	26.60	15.63	3.00
PE387	497	8	28	64	7	19.92	28.57	1.61
PE425	500	19	49	75	1	25.00	38.78	3.80
PE1528	500	13	52	52	4	21.60	25.00	2.60
PE1614	500	25	57	118	22	39.40	43.86	5.00
PE1680	500	21	56	71	14	28.20	37.50	4.20
UL63	499	7	42	34	58	26.85	16.67	1.40
UL245	499	3	20	40	55	23.05	15.00	0.60
UL851	499	1	88	19	12	23.85	1.14	0.20
UL1095	500	8	107	17	25	29.80	7.48	1.60
UL1230	500	3	73	22	63	31.60	4.11	0.60

282